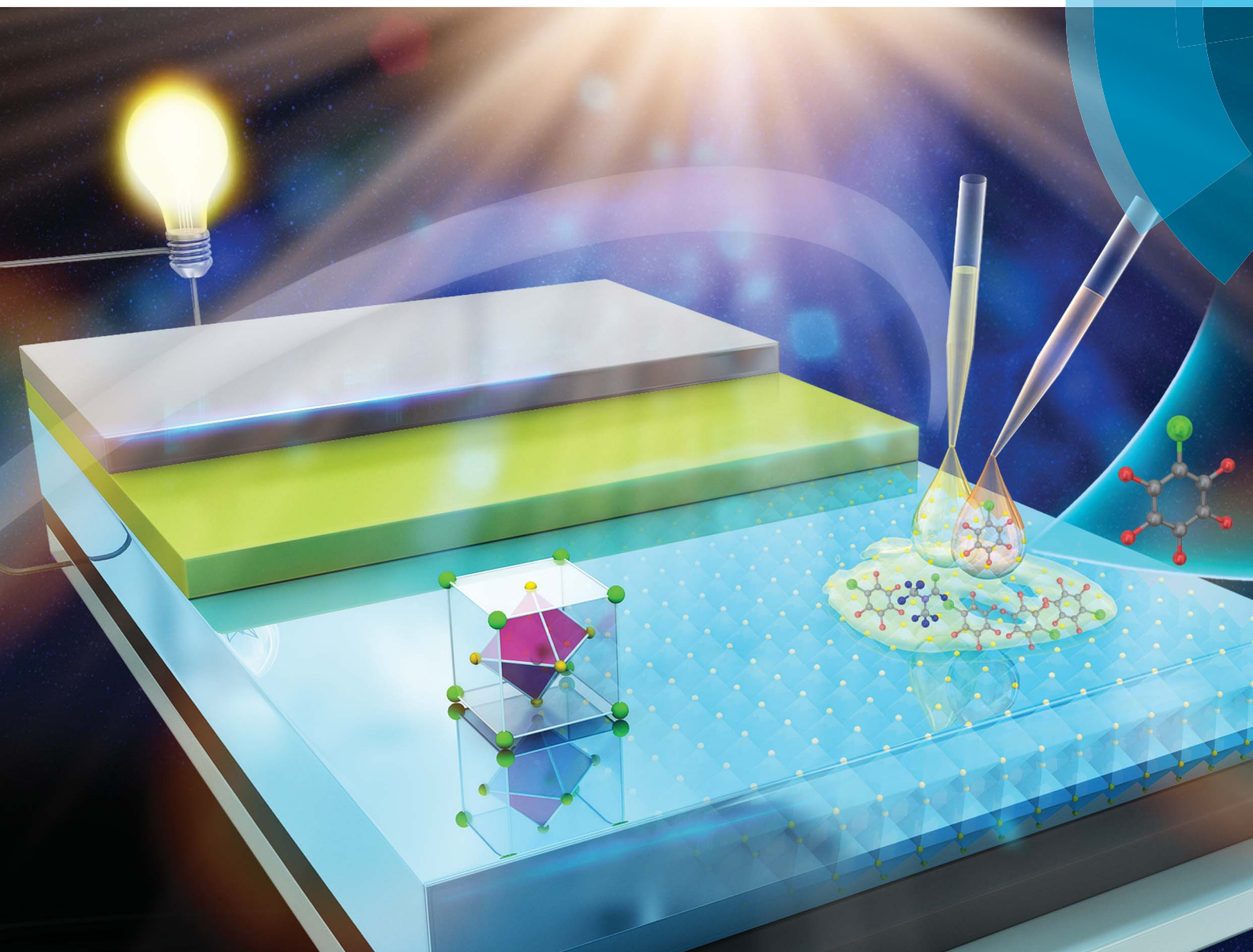


# Journal of Materials Chemistry A

Materials for energy and sustainability

[www.rsc.org/MaterialsA](http://www.rsc.org/MaterialsA)



ISSN 2050-7488



PAPER

Zhaoxin Wu *et al.*

Formation of ultrasmooth perovskite films toward highly efficient inverted planar heterojunction solar cells by micro-flowing anti-solvent deposition in air

**175** YEARS

Cite this: *J. Mater. Chem. A*, 2016, 4, 6295

# Formation of ultrasmooth perovskite films toward highly efficient inverted planar heterojunction solar cells by micro-flowing anti-solvent deposition in air<sup>†</sup>

Bin Xia,<sup>‡a</sup> Zhaoxin Wu,<sup>‡\*a</sup> Hua Dong,<sup>a</sup> Jun Xi,<sup>a</sup> Wen Wu,<sup>a</sup> Ting Lei,<sup>a</sup> Kai Xi,<sup>c</sup> Fang Yuan,<sup>a</sup> Bo Jiao,<sup>a</sup> Lixin Xiao,<sup>b</sup> Qihuang Gong<sup>b</sup> and Xun Hou<sup>a</sup>

Ultrasmooth perovskite thin films are prepared by a solution-based one-step micro-flowing anti-solvent deposition (MAD) method carried out in air with simplicity and practicability. Engaging inert gas blow and anti-solvent drips as accelerators, ultrafast crystallizing, thickness controllable, and high quality methylammonium lead iodide films are prepared with a least root mean square roughness of 1.43 nm (1.95 nm on average), achieving the smoothest surface morphology to the best of our knowledge, as well as a rather compact perovskite layer with a high coverage ratio. Perovskite films formed from MAD require no annealing procedure to ultimately crystallize, realizing a very fast crystallizing procedure within few seconds. By controlling the thickness of perovskite films, superior photovoltaic performance of solar cells with a large fill factor of 0.8 and a PCE of 15.98% is achieved without a glovebox. MAD technology will benefit not only highly efficient photovoltaic devices, but also perovskite-based hybrid optoelectronic devices with field effect transistors and light emitting diodes as well.

Received 10th January 2016  
Accepted 1st March 2016

DOI: 10.1039/c6ta00253f

[www.rsc.org/MaterialsA](http://www.rsc.org/MaterialsA)

## 1 Introduction

Thin film photovoltaic devices have great potential to take advantage of clean renewable energy.<sup>1</sup> Organometal halide perovskite solar cells have been put in the spotlight since the incipient work of Miyasaka *et al.*<sup>2</sup> In six years, tremendous progress of power conversion efficiency (PCE) from 3.8% to 20.1% has been made in organometal lead halide perovskite solar cells due to their high efficiencies as well as low-cost and ease of fabrication.<sup>3–7</sup> To enhance the PCE of perovskite solar cells, much research has been conducted on the structure of devices and on the choice of charge transport materials.<sup>8–10</sup> Most efficient perovskite solar cells used the regular configuration, which engaged mesoscopic metal oxides such as TiO<sub>2</sub>, Al<sub>2</sub>O<sub>3</sub>, and ZrO<sub>2</sub>, requiring a high-temperature sintering procedure at 500 °C.<sup>11–13</sup> The inverted configuration with

planar architecture, on the other hand, employed organic transport layers that could be easily deposited at low temperature with economy and practicability,<sup>9,10</sup> albeit the PCE of this kind of configuration was not as high as that of the regular one. Despite the importance of suitable device structures and other functional materials, preparation of smooth, consecutive and homogeneous planar perovskite films would be a primordial scenario to avoid shunting and recombination, so as to achieve high performance practically. Solution-based deposition is the most broadly applied technique to form relatively smooth and consecutive functional films, especially perovskite thin films, in organometal halide perovskite photovoltaic devices due to its simplicity and practicability. Original one-step deposition as an easy way to prepare perovskite films was adopted widely, but those perovskite films prepared by this method suffered from relatively low coverage and consecutiveness which resulted in shunting and recombination of carriers in solar cells.<sup>14</sup> Additives such as 1,8-diiodooctane (DIO) or 1-chloronaphthalene (CN) commingled with a one-step perovskite precursor could improve the morphology of perovskite films to some extent, nevertheless, there were still obvious pinholes remaining in the perovskite films due to their relatively slow crystallization speed in high boiling point solvent *N,N*-dimethylformamide (DMF) (boiling point at 153 °C).<sup>15,16</sup> Compared with the films formed from one-step deposition, an almost all-covered perovskite film could be obtained by sequential

<sup>a</sup>Key Laboratory of Photonics Technology for Information, Key Laboratory for Physical Electronics and Devices of the Ministry of Education, School of Electronic and Information Engineering, Xi'an Jiaotong University, Xi'an, 710049, P. R. China. E-mail: zhaoxinwu@mail.xjtu.edu.cn; Tel: +86-29-82664867

<sup>b</sup>State Key Laboratory for Mesoscopic Physics and Department of Physics, Peking University, Beijing, 100871, P. R. China

<sup>c</sup>Department of Materials Science and Metallurgy, University of Cambridge, Cambridge, CB2 3QZ, UK

<sup>†</sup> Electronic supplementary information (ESI) available. See DOI: 10.1039/c6ta00253f

<sup>‡</sup> These authors contributed equally to this work.

deposition.<sup>14</sup> Although the problem of coverage and consecutiveness was well solved by sequential deposition, the film roughness from sequential deposition was rather high due to acute dipping reactions and large crystal sizes, which made it difficult for the perovskite layers to be fully covered by the hole transport layer (HTL) or the electron transport layer (ETL), thus leading to carrier recombination in devices and deterioration of their performance.<sup>17,18</sup> Compact and consecutive perovskite films prepared by advanced deposition methods, such as one-step deposition engaging lead acetate (PbAc<sub>2</sub>) and solvent engineering, possessed excellent surface morphology.<sup>19,20</sup> However, the same as most of the solution deposition methods, they needed a nitrogen-filled glovebox, which added complexity to the fabrication and operation process. Vapor deposition, another kind of method different from solution deposition, enabled perovskite films to have high qualities such as flatness, homogeneity, and high coverage.<sup>21,22</sup> But inevitably, vapor deposition required a sophisticated vacuum system and *in situ* surveillance over the deposition rate,<sup>23</sup> which might not adapt to the tide of economically low-cost and practically easy-fabrication in the perovskite solar cell industry in the future. Compared with vapor deposition, solution deposition had its advantages of simplicity and practicability. Nevertheless, either conventional one-step deposition or sequential deposition left perovskite films with morphology defects which could not be made up easily, and advanced deposition methods needed a glovebox to ensure the quality of perovskite films in most cases.

Herein, we report a solution-based one-step micro-flowing anti-solvent deposition (MAD) process carried out in ambient atmosphere with simplicity and practicability. The term “micro” does not mean the exact magnitude of millionth. Instead, “micro” here is a description which indicates the moderate flow of N<sub>2</sub> gas with neither high pressure nor strong intensity. “Micro-flowing” is an assistant process together with “anti-solvent” to accelerate the evaporation rate of the solvent. When an anti-solvent was added to the substrate during spin-coating, the N<sub>2</sub> gas moderately flowed over the substrate, facilitating the evaporation of the solvent and the crystallization of perovskite films. Engaging anti-solvent and inert gas blow as accelerators, ultrafast crystallizing, thickness controllable, and high quality methylammonium lead iodide (CH<sub>3</sub>NH<sub>3</sub>PbI<sub>3</sub>) films were prepared with an average root mean square (RMS) roughness less than 2 nm and nonporous coverage. Compared to either one-step deposition, sequential deposition or vapor deposition, perovskite films prepared by MAD possessed the smoothest surface morphology to the best of our knowledge, as well as a rather compact perovskite layer with a high coverage ratio. Moreover, perovskite films formed from MAD required no annealing procedure to ultimately crystallize, realizing a real ultrafast procedure within a few seconds. By controlling the thickness of the perovskite films and optimizing the ETL, superior photovoltaic performance of solar cells with a large fill factor (FF) near 0.8 and a PCE of 15.98% was achieved without a glovebox.

## 2 Experimental section

### 2.1 Materials

Aqueous dispersions of PEDOT:PSS (CLEVIOS PVP Al 4083) were obtained from Heraeus and used as received. PbI<sub>2</sub> (99.999 wt%) was purchased from Alfa Aesar and used as received. CH<sub>3</sub>NH<sub>3</sub>I was prepared similar to a previously published method,<sup>11</sup> in brief: 24 mL methylamine solution (33 wt% in ethanol, Sigma Aldrich) and 10 mL hydriodic acid (57 wt% in water, Sigma Aldrich) were diluted by using 100 mL ethanol in a 250 mL round bottom flask by constant stirring at 0 °C for 2 hours. The precipitate of CH<sub>3</sub>NH<sub>3</sub>I was obtained by rotary evaporation at 40 °C and washed with dry diethyl ether until the solid became white. The final product was dried at 60 °C in a vacuum oven for 24 hours. PC<sub>61</sub>BM (99.5%) and PC<sub>71</sub>BM (99.5%) were both purchased from Solenne and used as received.

### 2.2 Perovskite-based solar cell fabrication

ITO glass substrates were sequentially cleaned with detergent, acetone and deionized water, and were dried at last. Dry ITO glass substrates were treated with ultraviolet ozone plasma for 5 minutes for further cleaning. PEDOT:PSS solution was spin-coated on ITO glass at 2500 rpm for 30 seconds and annealed at 140 °C for 10 minutes, forming a PEDOT:PSS layer of 45 nm. After annealing, a DMF solution of CH<sub>3</sub>NH<sub>3</sub>PbI<sub>3</sub> (CH<sub>3</sub>NH<sub>3</sub>I and PbI<sub>2</sub> in 1 : 1 molar ratio) was spin-coated on the substrate at 5000 rpm for 60 seconds with an 800 L h<sup>-1</sup> dry nitrogen gas flow blowing over the film 5 seconds before spin-coating till the end of it. To realize a homogeneous perovskite film, a gas flow meter and a funnel were engaged. The gas flow meter was linked between the N<sub>2</sub> gas cylinders to control the speed of the N<sub>2</sub> flow to a moderate extent to realize “micro-flowing” and the funnel right above the substrate could help to disperse the N<sub>2</sub> flow at almost the same rate in different directions. During the spinning, few drops of chlorobenzene were quickly added to the film at a certain time (*e.g.* the 4th second for 35 wt% CH<sub>3</sub>NH<sub>3</sub>PbI<sub>3</sub> in DMF solution) after the beginning of spin-coating for a CH<sub>3</sub>NH<sub>3</sub>PbI<sub>3</sub> in DMF solution. 20 mg mL<sup>-1</sup> PC<sub>61</sub>BM or PC<sub>71</sub>BM in chlorobenzene was then spin-coated on the perovskite film at 2000 rpm or 3000 rpm respectively for 30 seconds, and was annealed at 80 °C for 10 minutes to form a 30 nm electron transport layer. All of the spin-coating procedures were carried out in ambient atmosphere. 10 nm BCP and 140 nm Ag were thermally evaporated onto the PCBM layer to eventually consummate the device.

### 2.3 Characterization

The absorption and transmittance spectra were acquired by using a UV-vis spectrophotometer (Fluoromax 4, HORIBA Jobin Yvon, USA). Crystalline structures were performed by X-ray diffraction (XRD) (D/MAX-2400, Rigaku, Japan) with Cu K $\alpha$  radiation. Surface morphology was investigated by scanning electron microscopy (SEM) (Quanta 250, FEI) and atomic force microscopy (AFM) (Solver P47H-PRO, NT-MDT, Russia). Device characteristics were evaluated in ambient under an AAA solar simulator (XES-301S, SAN-EI Electric. Co. Ltd.), AM 1.5G

illumination with an intensity of  $100 \text{ mW cm}^{-2}$  (1 sun, calibrated by a NREL-traceable KG5 filtered silicon reference cell). Meanwhile, the current density–voltage ( $J$ – $V$ ) curves were measured by using a Keithley digital source meter (Model 2602). The scan rate of the planar heterojunction perovskite solar cell current–voltage curves was  $0.05 \text{ V s}^{-1}$ . Incident photon-to-current conversion efficiency (IPCE) spectra were obtained by using the solar cell quantum efficiency measurement system (SolarCellScan 100, Zolix instruments. Co. Ltd.). The area of each device, calibrated by the shadow mask, was  $9.00 \text{ mm}^2$ .

## 3 Results and discussion

### 3.1 Perovskite film formation and characterization

The perovskite thin films were prepared by the MAD method in ambient atmosphere as shown in Fig. 1a and S1.† All detailed processes can be found in the Experimental section. Drops of DMF solution of  $\text{CH}_3\text{NH}_3\text{PbI}_3$  (35 wt%) were spin-coated on the substrate at 5000 rpm for 60 seconds with an  $800 \text{ L h}^{-1}$  dry

nitrogen gas ( $\text{N}_2$ ) flow blowing over the film 5 seconds before spinning till the end of it. During the spinning, few drops of chlorobenzene were quickly added to the film at a certain time, the 4th second for example, after the beginning. The  $\text{N}_2$  flow acted as an accelerator that enabled DMF to evaporate quickly and formed a saturated solution within few seconds during the incipient stage of spinning. Then, the role of chlorobenzene was to rapidly reduce the solubility of  $\text{CH}_3\text{NH}_3\text{PbI}_3$  in the saturated solution and to bring about ultrafast nucleation, precipitation, and formation of the crystals in the film.<sup>24</sup> During the rest time of spin-coating, DMF and chlorobenzene either evaporated quickly under the  $\text{N}_2$  flow or deviated from the substrate dissolved in each other. When spin-coating was over, there was hardly DMF and chlorobenzene remnant on the perovskite film and the film was crystallized ultimately without the annealing process. Fig. S2† shows the absorption of perovskite films deposited by MAD with and without the annealing process. There was hardly any difference between the two curves, suggesting that perovskite crystals formed completely during the

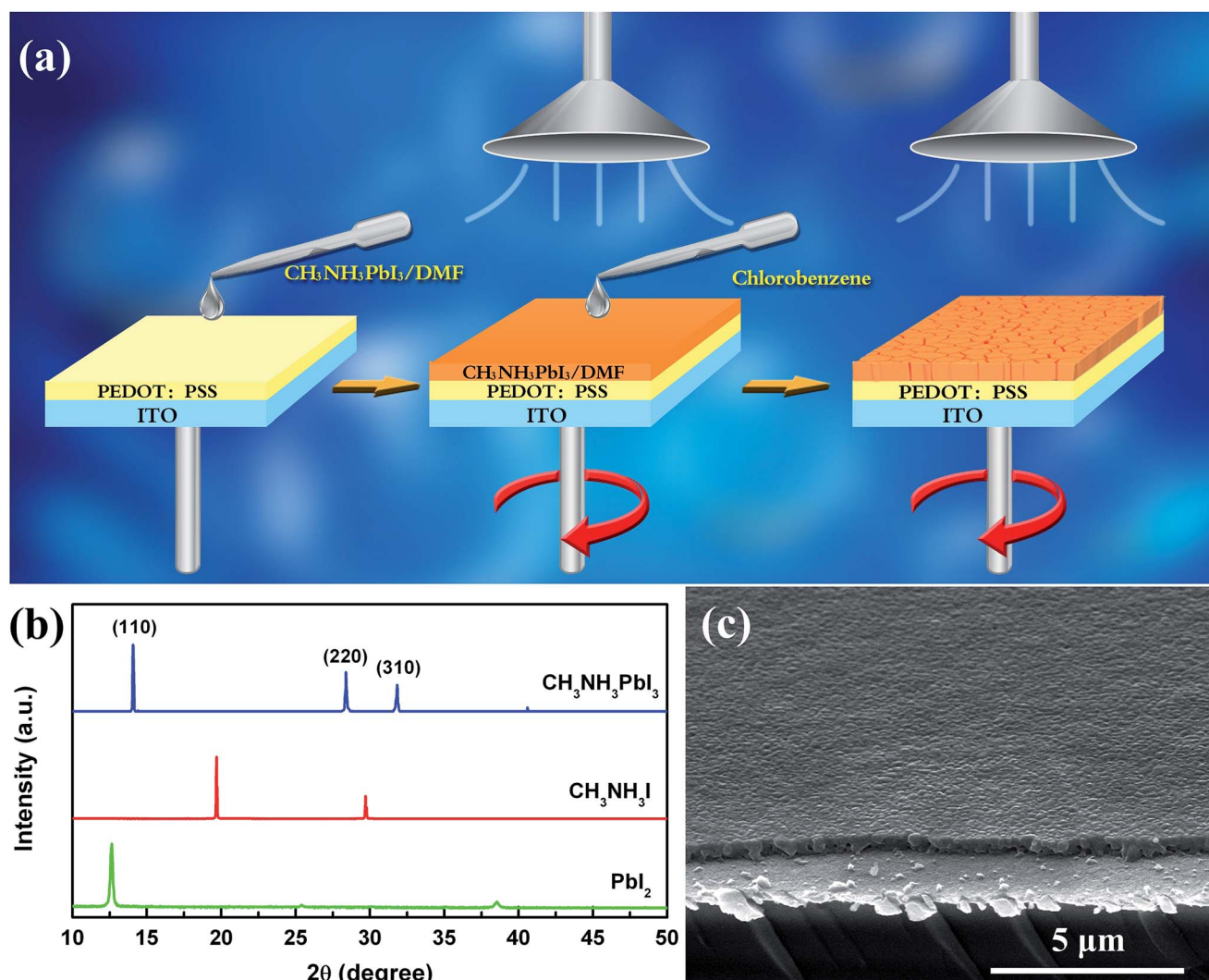


Fig. 1 (a) Schematic procedure for the MAD method progressing from left to right. (b) XRD patterns of the  $\text{CH}_3\text{NH}_3\text{PbI}_3$  perovskite film,  $\text{CH}_3\text{NH}_3\text{I}$  film and  $\text{PbI}_2$  film. (c) Tilt-angle SEM image of the perovskite thin film prepared by MAD.

spin-coating. Perovskite films without the annealing procedure were further characterized by X-ray diffraction (XRD) patterns shown in Fig. 1b.

Clear diffraction peaks at  $14.08^\circ$ ,  $28.40^\circ$ , and  $31.83^\circ$  can be respectively assigned to (110), (220), and (310) planes as the diffraction of the tetragonal  $\text{CH}_3\text{NH}_3\text{PbI}_3$  phase. No diffraction peaks of  $\text{PbI}_2$  or  $\text{CH}_3\text{NH}_3\text{I}$  were found in the curve of  $\text{CH}_3\text{NH}_3\text{PbI}_3$  crystals, indicating that the entire compound reacted completely during MAD even without the annealing process. XRD patterns of perovskite films with different thicknesses corresponding to different concentrations of  $\text{CH}_3\text{NH}_3\text{PbI}_3$  are shown in Fig. S3.† XRD patterns of perovskite films with different thicknesses revealed the complete reaction and tetragonal crystal phase, which, to a great extent, meant the independence of solution concentrations in the MAD. Scanning electron microscopy (SEM) images of surface morphology in Fig. 1c and 2a and b demonstrate that perovskite crystals were packed densely without pinholes, resulting in a homogeneous film with a quite complete coverage. Since the  $\text{N}_2$  flow rate was almost the same in different directions, the crystallization conditions of perovskite in different positions on the substrate were almost the same. As can be seen in Fig. S4,† five areas of the perovskite film on one substrate were characterized by SEM. Perovskite grain sizes were

almost homogeneous from areas (a) to (e), indicating almost the same  $\text{N}_2$  flow rate at different directions and positions.

During the MAD, the moment of chlorobenzene addition is vital to the surface morphology of perovskite films. For solution of a certain concentration, 35 wt% for example, crystals precipitated at only the 4th second after the beginning of spin-coating with the solution turning vague and opaque rapidly and obviously due to the acceleration effect of  $\text{N}_2$  flow. Chlorobenzene should be added right half a second earlier before crystal precipitation. Chlorobenzene added too early (*e.g.* at the 2nd second after the beginning of spin-coating) resulted in a rod-like film morphology that was similar to the morphology of films prepared by conventional one-step deposition (Fig. 2c and d).<sup>13</sup> This kind of rod-like morphology was probably ascribed to the unsaturated  $\text{CH}_3\text{NH}_3\text{PbI}_3$  solution in which colloid-based growth was the dominating way of crystallization, in accordance with the perovskite colloidal chemical study carried out previously by another group.<sup>25</sup> By colloid-based growth, disk-like particles up to *ca.* 200 nm in size were yielded and packed in lines towards different directions, devastating the consecutiveness of the film. On the other hand, adding chlorobenzene too late (*e.g.* at the 5th second after the beginning of spin-coating) resulted in a morphology in which rod-like composition seemed

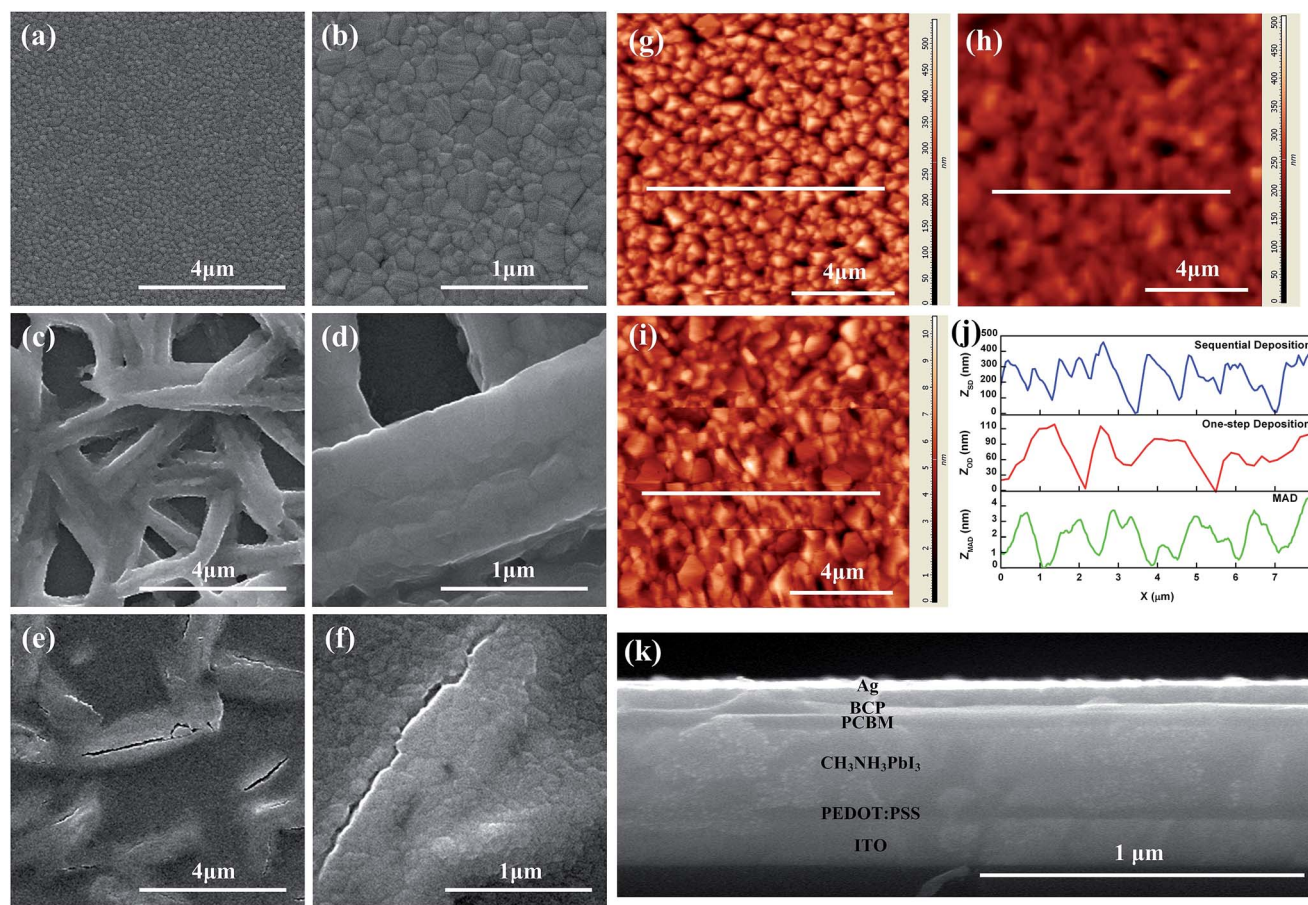


Fig. 2 SEM images of perovskite films with chlorobenzene added at (a) and (b) right moment, (c) and (d) early moment and (e) and (f) late moment. AFM images and RMS analyses (j) of perovskite films made by (g) sequential deposition (SD), (h) one-step deposition (OD) and (i) MAD, respectively. Cross-sectional SEM image of the full device (k).

to be buried in compact perovskite particles (Fig. 2e and f). This unique morphology might have arisen from the over-saturated solution and the simultaneous existence of both colloid-based growth and solution-based growth when  $\text{CH}_3\text{NH}_3\text{PbI}_3$  was crystallizing.<sup>25</sup> Colloid-based growth yielded rod-like morphology and solution-based growth yielded compact particle morphology, respectively. Adding chlorobenzene at half a second before the film turned opaque can make  $\text{CH}_3\text{NH}_3\text{PbI}_3$  crystallize at the right moment when the solution is neither unsaturated nor over-saturated, ensuring all solution-based growth in just-saturated solution during crystallization and yielding homogeneous morphology with compact particles (Fig. 2a and b).

We further characterized perovskite films by atomic force microscopy (AFM), as shown in Fig. 2g–j. The RMS roughness of perovskite films prepared from sequential deposition, one-step deposition and MAD was calculated to be 75.5 nm, 42.6 nm, and 1.43 nm, respectively, for an area of  $10\ \mu\text{m} \times 10\ \mu\text{m}$  (Fig. 2j). It is worth emphasizing that not all of “pinholes” in those AFM images were real ones. In Fig. 2g and h corresponding to films prepared by sequential deposition and one-step deposition, respectively, those black pinholes were the real ones that directly led to the substrate through perovskite films. The depths of those pinholes could be confirmed from the AFM height coordinate that was in accordance with the film thickness (Fig. S5a and b†). In the AFM image of the perovskite film prepared by MAD (Fig. 2i), however, “black pinholes” were not the real ones since their depths were far less than the thickness of the film (Fig. S5c†). These pseudo-pinholes were only small fluctuations on the surface of the film, and they, in another aspect, demonstrated the good coverage of the smooth film. To investigate the reproducibility of MAD, a batch of 10 perovskite films were prepared under the same conditions. Characterized by AFM, their RMS roughnesses were analyzed and are shown in Table 1. An average RMS roughness of 1.95 nm indicated good reproducibility of ultrasoft surface morphology by the MAD method.

A relatively high speed of  $\text{N}_2$  flow is an essential factor to achieve such a smooth surface morphology.<sup>26</sup> Actually, under a low speed of  $\text{N}_2$  flow of  $400\ \text{L h}^{-1}$ , the solvent evaporated slowly, facilitating the migration of the solute in solution and leading to heterogeneous protruded crystals as well as pinholes (Fig. S6†). However, with a relatively high speed of  $\text{N}_2$  flow of  $800\ \text{L h}^{-1}$ , the solvent evaporated quickly in a relatively short time before solute migration, hence the film formed smoothly with neither protruded crystals nor pinholes. In MAD, the  $\text{N}_2$  blow acted more as an accelerator for quick volatilization, saturation, and crystallization than as a protective gas that excluded

moisture and oxygen. For comparison, perovskite films prepared in a  $\text{N}_2$ -filled glovebox with only chlorobenzene and without  $\text{N}_2$  blow were characterized as well (shown in Fig. S7†). In a glovebox with  $\text{N}_2$  acting as a protector alone, the perovskite film with chlorobenzene had a RMS surface roughness of 12.4 nm, far larger than that of the film prepared with a high speed  $\text{N}_2$  blow in ambient atmosphere. This might also be ascribed to the migration of ions in solution that resulted in overgrown crystals and pinholes. In this way,  $\text{N}_2$  blow in ambient atmosphere is not only merely a substitution of the glovebox, but also a much better access to achieve preminent film surface morphology. To the best of our knowledge, films prepared by solution-based MAD have the least surface RMS roughness to date, even compared with films prepared by vapor deposition or flash evaporation.<sup>21–23</sup>

### 3.2 Perovskite-based devices

To investigate the effect of perovskite films prepared by the MAD method, several batches of perovskite-based solar cells with MAD perovskite films of different thicknesses were fabricated. Every batch of devices contained 16 devices and they were all fabricated and characterized in ambient atmosphere except for the thermally evaporated silver cathode. The cross sectional SEM image of the planar heterojunction solar cell is shown in Fig. 2k. The inverted configuration consists of ITO coated glass, a hole transport layer of poly(3,4-ethyl-enedioxythiophene):poly(styrenesulfonic acid) (PEDOT:PSS), a micro-flowing anti-solvent deposited  $\text{CH}_3\text{NH}_3\text{PbI}_3$  perovskite absorber, an electron transport layer of (6,6)-phenyl- $\text{C}_{61}$ -butyric acid methyl ester ( $\text{PC}_{61}\text{BM}$ ), a hole blocking layer of 2,9-dimethyl-4,7-diphenyl-1,10-phenanthroline (BCP), and thermally evaporated silver contact (ITO/PEDOT:PSS/ $\text{CH}_3\text{NH}_3\text{PbI}_3$ /PCBM/BCP/Ag). The performance of devices employing perovskite films with different thicknesses was investigated under AM 1.5G illumination, and is shown in Fig. 3 and is summarized in Table 2. Different perovskite film thicknesses of 130 nm, 200 nm, 350 nm, 420 nm and 500 nm corresponded to  $\text{CH}_3\text{NH}_3\text{PbI}_3$  solution concentrations of 15 wt%, 25 wt%, 35 wt%, 45 wt% and 55 wt% during MAD, respectively, as shown in Fig. 4.

For devices with perovskite films from 130 nm to 350 nm, the short circuit current density ( $J_{\text{sc}}$ ) increased from  $18.35\ \text{mA cm}^{-2}$  to  $21.12\ \text{mA cm}^{-2}$  with the increase of thickness (Fig. 3a). This trend was in agreement with the film's absorption spectra and the incident photon-to-current conversion efficiency (IPCE) curves shown in Fig. 3b and d, respectively. Owing to the full coverage of perovskite films, the absorbance of light increased almost linearly with the increase of the perovskite film thickness. It demonstrated a broad range in the visible spectrum with the local maximum at 400 nm and the absorption onset at 780 nm, corresponding to the 1.55 eV band gap for this material. From the transmittance spectra in Fig. 3c, we found that when the film thickness reached 350 nm, no more than 5% of the light with wavelength less than 580 nm could pass through the film. And almost no transmittance in the wavelength range of 300–550 nm, where strong absorption occurs, indicated a high light utilization efficiency of perovskite films prepared by

Table 1 Average RMS roughness of 10 perovskite films prepared by MAD

Individual RMS roughness (nm)					Average RMS roughness (nm)
2.11	1.63	1.59	3.45	1.64	1.95
1.85	1.43	2.25	1.78	1.82	

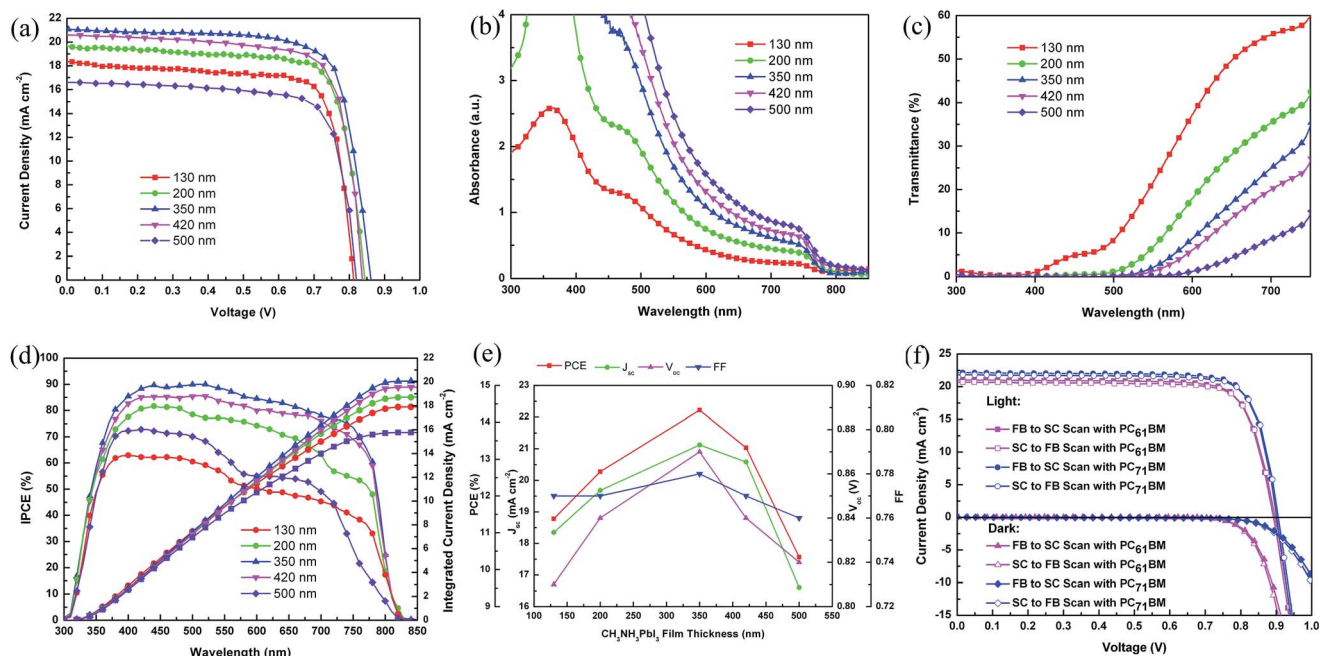


Fig. 3 (a)  $J$ - $V$  curves of perovskite-based devices. (b) UV-vis absorption spectra of MAD perovskite films. (c) UV-vis transmittance spectra of MAD perovskite films. (d) IPCE curves of perovskite-based devices. (e) PCE,  $J_{sc}$ ,  $V_{oc}$  and FF as functions of perovskite films with different perovskite film thicknesses. (f) Best performance of devices with PC<sub>61</sub>BM or PC<sub>71</sub>BM layers in different scan directions.

Table 2 Average and standard deviation photovoltaic parameters of solar cells with different perovskite film thicknesses. Parameters of each group with a certain perovskite film thickness were based on 16 devices

CH <sub>3</sub> NH <sub>3</sub> PbI <sub>3</sub> (nm)	$J_{sc}$ (mA cm <sup>-2</sup> )	$V_{oc}$ (V)	FF	PCE (%)	$R_s$ (Ω cm <sup>2</sup> )	$R_{sh}$ (Ω cm <sup>2</sup> )
130	18.35 ± 0.05	0.81 ± 0.02	0.77 ± 0.02	11.38 ± 0.15	1.03 ± 0.04	303 ± 5.79
200	19.68 ± 0.06	0.84 ± 0.03	0.77 ± 0.01	12.66 ± 0.14	1.40 ± 0.03	284 ± 4.95
350	21.12 ± 0.03	0.87 ± 0.02	0.78 ± 0.01	14.33 ± 0.10	1.76 ± 0.02	342 ± 4.22
420	20.58 ± 0.05	0.84 ± 0.04	0.77 ± 0.03	13.31 ± 0.19	1.32 ± 0.04	295 ± 5.34
550	16.60 ± 0.09	0.82 ± 0.06	0.76 ± 0.04	10.34 ± 0.23	1.31 ± 0.08	257 ± 7.28

MAD from another aspect. Thus, there might be a large amount of photo-generated carriers offering the potential to achieve a high  $J_{sc}$  for the device with thick perovskite films. However, when the thickness of perovskite films reached 420 nm and 500 nm,  $J_{sc}$  decreased severely to 20.58 mA cm<sup>-2</sup> and 16.61 mA cm<sup>-2</sup>, respectively (Fig. 3e). Although the absorption with perovskite films of 420 nm and 500 nm was higher than that below 350 nm, and the transmittance spectra curves of thick films were even lower, photo-generated carriers were probably confined to *ca.* 100 nm diffusion length in CH<sub>3</sub>NH<sub>3</sub>PbI<sub>3</sub>,<sup>27</sup> limiting the quantum yield for the electron injection and electron collection efficiency.<sup>28</sup> Additionally, it can be calculated from SEM images that the average particle size did not increase linearly with perovskite film thickness (Fig. 4). When the perovskite films had thicknesses no more than 350 nm, average particle sizes were similar to or slightly less than the film thickness, meaning that there was basically only one layer of compact particles in the film. When the film thicknesses were beyond 350 nm, average particle sizes did not augment to the

extent where they commensurate with the film thicknesses, suggesting that thick perovskite films consisted of more than one layer of compact particles. This situation could be confirmed from the cross sectional SEM images shown in Fig. 2k and 4. Having more than one perovskite particle layer presumably made photo-generated carriers encounter more grain boundaries in thicker films with more recombination, and thusly, made them harder to be completely transported to and collected by charge transport layers. Unfortunately, although there was almost one single layer of particles in films thinner than 350 nm without much grain boundaries for photo-generated carriers to encounter, the absorbance of light for such a thin film was not enough to generate a large amount of carriers to achieve a high  $J_{sc}$ . On this account, a further decrease of perovskite film thickness from 350 nm to 130 nm reduced the light absorbance and  $J_{sc}$ , while a further increase of them from 350 nm to 500 nm resulted in a declined  $J_{sc}$  and  $V_{oc}$  as well.

The FF of devices with different perovskite films thickness, however, remained at a relatively stable and high level near 0.8.

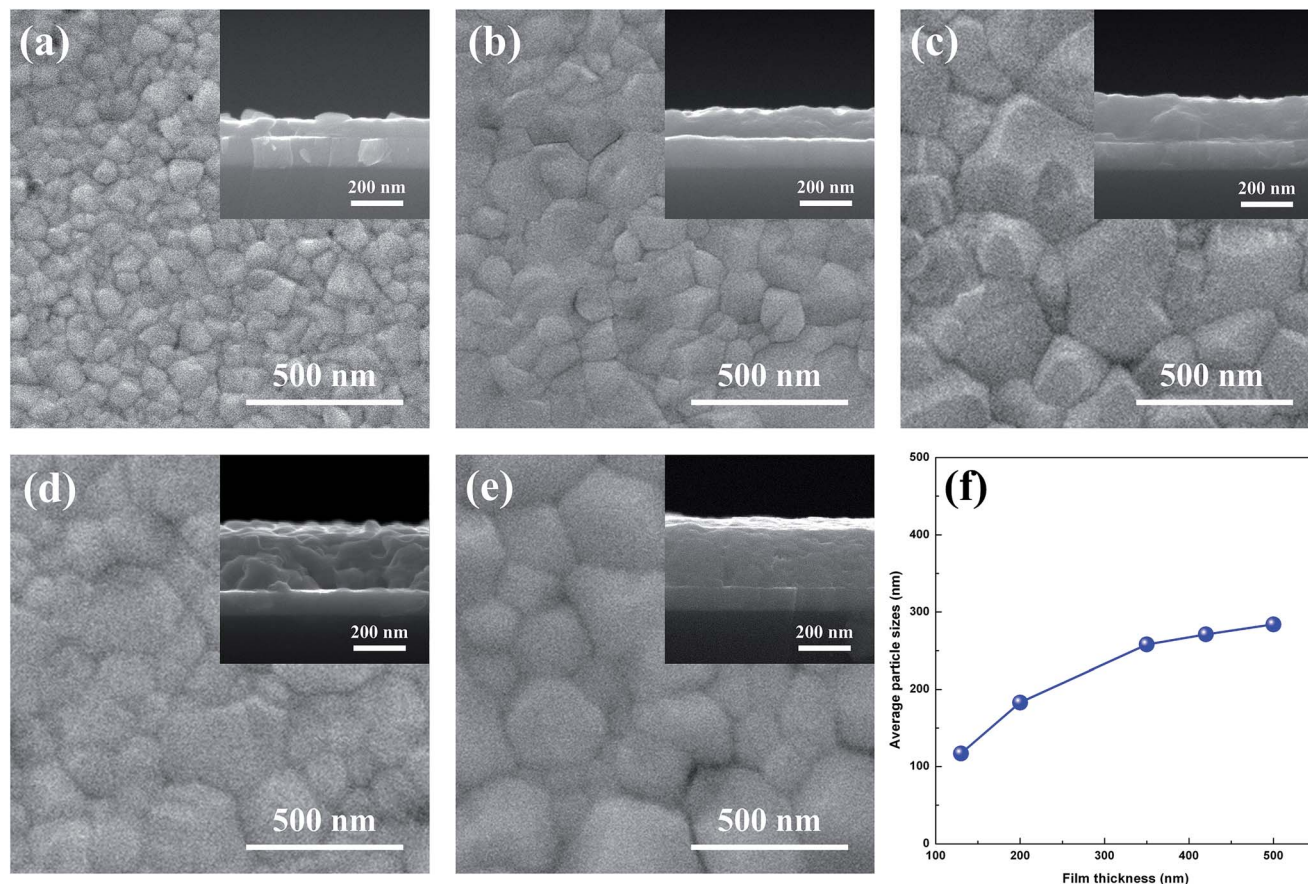


Fig. 4 Average particle sizes with different perovskite film thicknesses. The insets show the cross-sectional SEM images of perovskite films with increasing thickness on a 180 nm substrate.

The value of the FF reflected the existence of interface state corresponding to electrical and electrochemical losses, which can be estimated by the series resistance ( $R_s$ ) and shunt resistance ( $R_{sh}$ ).<sup>28</sup> Devices with low  $R_s$  and high  $R_{sh}$  have good interfacial contact and less electrical and electrochemical losses, leading to a high FF. For our devices with different perovskite film thickness, the series resistance ( $R_s$ ) could be obtained by linearly fitting from the  $J$ - $V$  curves around the point  $J = 0$  mA  $\text{cm}^{-2}$ , and the shunt resistance ( $R_{sh}$ ) could be extracted around the point  $V = 0$  V.<sup>29</sup> The results are listed in Table 2. With different thicknesses of perovskite films,  $R_s$  varied only from 1.01  $\Omega \text{ cm}^2$  to 1.96  $\Omega \text{ cm}^2$ , which was in a relatively low level and  $R_{sh}$  fluctuated around 300  $\Omega \text{ cm}^2$ , in accordance with smooth and full coverage surface morphology. Owing to the superior film morphology from MAD with low RMS roughness and full coverage, good interface contact between perovskite films and charge transport layers was obtained. Few defects and less charge carrier recombination at interfaces were favorable for photo-generated carrier collection, which led to a relatively high FF. Given a relatively stable FF, the PCE of devices was mainly affected by parameters of  $J_{sc}$  and  $V_{oc}$ , making the average PCE around 14.33% with a 350 nm perovskite film (Fig. 3e). The best device performance shown in Fig. 3f exhibited a  $J_{sc}$  of 21.02 mA  $\text{cm}^{-2}$ , a  $V_{oc}$  of 0.89 V, a FF of 0.796, and a PCE of 14.89% with

only 3% hysteresis between forward bias to short circuit (FB-SC) scan and short circuit to forward bias (SC-FB) scan.

To investigate the impact of air and the annealing process on perovskite films and the whole devices, we compared the absorption of perovskite films prepared by the MAD method in four different environmental conditions: perovskite films prepared in air without the annealing process, perovskite films prepared in air with the annealing process, perovskite films prepared in the glovebox without the annealing process and perovskite films prepared in the glovebox with the annealing process. Except for the different environmental conditions and the annealing process, all the other conditions were the same during preparation procedures, and the thickness of perovskite films was 350 nm. The absorption spectra of these four kinds of perovskite films are shown in Fig. S8.† From Fig. S8,† we could hardly figure out the difference between these perovskite films prepared in air and glovebox as well as whether they were annealed or not. These curves indicated that the films prepared by the MAD method had good air stability, and the annealing process had almost no impact on them. Then we compared the performance of solar cells engaging these four kinds of perovskite films, as shown in Fig. S9 and summarized in Table S1.† The PCEs of four kinds of devices were 14.58%, 14.63%, 14.41% and 14.32%, respectively.  $J_{sc}$ ,  $V_{oc}$  and FF were almost the same.

There was hardly any obvious enhancement in the devices with perovskite films prepared in a glovebox or with the annealing process. So we considered that annealing-free perovskite films prepared by the MAD method in air had good quality. The application of the glovebox and the annealing process would possibly not improve the performance of devices.

### 3.3 Device optimization

Once the optimal thickness of the perovskite film has been determined, the charge transport layer was optimized to find the best performing device. (6,6)-Phenyl-C<sub>71</sub>-butyric acid methyl ester (PC<sub>71</sub>BM) with a higher electron collection efficiency was used to replace PC<sub>61</sub>BM to enhance the photovoltaic performance of devices. A higher electron collection efficiency of PC<sub>71</sub>BM could be characterized and calculated by PL quenching measurements, shown in Fig. S10.† When 20 nm PC<sub>61</sub>BM was deposited on a perovskite film (glass/perovskite/PC<sub>61</sub>BM), PL quenched 87%, indicating that PC<sub>61</sub>BM had a good electron collection efficiency. As a contrast, when 20 nm PC<sub>71</sub>BM was deposited on the perovskite film (glass/perovskite/PC<sub>71</sub>BM), PL quenching reached 92%, demonstrating that PC<sub>71</sub>BM has a higher electron collection efficiency compared with PC<sub>61</sub>BM. PL quenching measurements illustrated a better performance of PC<sub>71</sub>BM as an ETL than that of PC<sub>61</sub>BM, and PC<sub>71</sub>BM with a better electron collection efficiency contributed to a better performance in solar cells, especially in terms of  $J_{sc}$ , as shown in Fig. 3f and Table 3. Different from the PC<sub>71</sub>BM thickness reported previously of about 140 nm,<sup>30,31</sup> we fabricated a PC<sub>71</sub>BM layer of only 20 nm because of the ultrasmooth perovskite layer in our devices. 20 nm PC<sub>71</sub>BM was thick enough to cover all the perovskite layer and thicker PC<sub>71</sub>BM would lead to a decrease of  $J_{sc}$  due to the longer way of electron transport. Devices with 350 nm perovskite films engaging 20 nm PC<sub>71</sub>BM as an electron transport layer demonstrated a higher performance than those with PC<sub>61</sub>BM. The best PCE of 15.98% with a  $J_{sc}$  of 22.14 mA cm<sup>-2</sup>, a  $V_{oc}$  of 0.90 V, and a FF of 0.802 was obtained along with PC<sub>71</sub>BM, showing better  $J_{sc}$ ,  $V_{oc}$ , and FF compared to those devices with PC<sub>61</sub>BM.

The device stability with PC<sub>71</sub>BM was measured without encapsulation. The stability characterization was based on a batch of 16 devices, and the average PCE of them is shown in Fig. S11.† At first, the average PCE of devices was 15.90%, while at the end of the test, the average PCE decreased to 14.82%. The devices showed considerable stability over 400 hours (about 16 days) and maintained 93% of its initial efficiency.

**Table 3** Best performance of devices with PC<sub>61</sub>BM or PC<sub>71</sub>BM layers in different scan directions

ETL	Scan direction	$J_{sc}$ (mA cm <sup>-2</sup> )	$V_{oc}$ (V)	FF	PCE (%)
PC <sub>61</sub> BM	FB–SC	21.02	0.89	0.796	14.89
	SC–FB	20.69	0.89	0.789	14.53
PC <sub>71</sub> BM	FB–SC	22.14	0.90	0.802	15.98
	SC–FB	21.80	0.90	0.795	15.60

## 4 Conclusions

In conclusion, ultrasmooth perovskite films with full coverage and superior surface morphology were fabricated by a novel one-step solution-based micro-flowing anti-solvent method in air. Perovskite films prepared by MAD were characterized by XRD, SEM, and AFM, exhibiting a complete deposition reaction, compact perovskite layers with full coverage, and the smoothest surface morphology to date. Devices engaging perovskite films prepared by MAD demonstrated strong light absorption with a relatively high  $J_{sc}$ . Superior surface morphology of perovskite films gave rise to a stably high FF near 0.80 with low  $R_s$  and high  $R_{sh}$ . By optimizing the electron transport layer, a PCE of 15.98% was obtained with negligible hysteresis between forward and backward  $J$ – $V$  scans and considerable device stability without encapsulation. We believe that this solution-based MAD technology will benefit highly efficient photovoltaic device fabrication with economically low-cost, operationally low-temperature, and practically easy-fabrication, as well as perovskite-based hybrid optoelectronic devices with field effect transistors and light emitting diodes.

## Acknowledgements

This work was financially supported by the Basic Research Program of China (2013CB328705), National Natural Science Foundation of China (Grant No. 11574248, 61275034), PhD Programs Foundation of Ministry of Education of China (Grant No. 20130201110065), and International Cooperation by Shaanxi (Grant No. 2015KW-008). The authors thank Professor Xiong Gong for his help in this work. The SEM work was carried out at International Center for Dielectric Research (ICDR), Xi'an Jiaotong University, Xi'an, China; the authors also thank Ms Dai for her help in using SEM.

## Notes and references

- 1 S. B. Darling and F. You, *RSC Adv.*, 2013, **3**, 17633.
- 2 A. Kojima, K. Teshima, Y. Shirai and T. Miyasaka, *J. Am. Chem. Soc.*, 2009, **131**, 6050.
- 3 H. J. Snaith, *J. Phys. Chem. Lett.*, 2013, **4**, 3623.
- 4 N. G. Park, *J. Phys. Chem. Lett.*, 2013, **4**, 2423.
- 5 P. Gao, M. Grätzel and M. K. Nazeeruddin, *Energy Environ. Sci.*, 2014, **7**, 2448.
- 6 S. Kazim, M. K. Nazeeruddin, M. Grätzel and S. Ahmad, *Angew. Chem., Int. Ed.*, 2014, **53**, 2812.
- 7 W. S. Yang, J. H. Noh, N. J. Jeon, Y. C. Kim, S. Ryu, J. Seo and S. Il Seok, *Science*, 2015, **348**, 1234.
- 8 P. Qin, S. Tanaka, S. Ito, N. Tetreault, K. Manabe, H. Nishino, M. K. Nazeeruddin and M. Grätzel, *Nat. Commun.*, 2014, **5**, 3834.
- 9 J. Y. Jeng, K. C. Chen, T. Y. Chiang, P. Y. Lin, T. D. Tsai, Y. C. Chang, T. F. Guo, P. Chen, T. C. Wen and Y. J. Hsu, *Adv. Mater.*, 2014, **26**, 4107.
- 10 J. Y. Jeng, Y. F. Chiang, M. H. Lee, S. R. Peng, T. F. Guo, P. Chen and T. C. Wen, *Adv. Mater.*, 2013, **25**, 3727.

- 11 M. M. Lee, J. Teuscher, T. Miyasaka, T. N. Murakami and H. J. Snaith, *Science*, 2012, **338**, 643.
- 12 J. M. Ball, M. M. Lee, A. Hey and H. J. Snaith, *Energy Environ. Sci.*, 2013, **6**, 1739.
- 13 A. Mei, X. Li, L. Liu, Z. Ku, T. Liu, Y. Rong, M. Xu, M. Hu, J. Chen, Y. Yang, M. Grätzel and H. Han, *Science*, 2014, **345**, 295.
- 14 N. Yantara, D. Sabba, F. Yanan, J. M. Kadro, T. Moehl, P. P. Boix, S. Mhaisalkar, M. Grätzel and C. Grätzel, *Chem. Commun.*, 2015, **51**, 4603.
- 15 P.-W. Liang, C.-Y. Liao, C.-C. Chueh, F. Zuo, S. T. Williams, X.-K. Xin, J. Lin and A. K.-Y. Jen, *Adv. Mater.*, 2014, **26**, 3748.
- 16 X. Song, W. Wang, P. Sun, W. Ma and Z.-K. Chen, *Appl. Phys. Lett.*, 2015, **106**, 033901.
- 17 L. Zheng, Y. Ma, S. Chu, S. Wang, B. Qu, L. Xiao, Z. Chen, Q. Gong, Z. Wu and X. Hou, *Nanoscale*, 2014, **6**, 8171.
- 18 H. Dong, Z. Wu, B. Xia, J. Xi, F. Yuan, S. Ning, L. Xiao and X. Hou, *Chem. Commun.*, 2015, **50**, 8986.
- 19 W. Zhang, M. Saliba, D. T. Moore, S. K. Pathak, M. T. Hörantner, T. Stergiopoulos, S. D. Stranks, G. E. Eperon, J. A. Alexander-Webber, A. Abate, A. Sadhanala, S. Yao, Y. Chen, R. H. Friend, L. A. Estroff, U. Wiesner and H. J. Snaith, *Nat. Commun.*, 2015, **6**, 6142.
- 20 N. J. Jeon, J. H. Noh, Y. C. Kim, W. S. Yang, S. Ryu and S. Il Seok, *Nat. Mater.*, 2014, **13**, 897.
- 21 M. Z. Liu, M. B. Johnston and H. J. Snaith, *Nature*, 2013, **301**, 395.
- 22 O. Malinkiewicz, C. R. Carmona, A. Soriano, E. Bandiello, L. Camacho, M. K. Nazeeruddin and H. J. Bolink, *Adv. Energy Mater.*, 2014, **4**, 1400345.
- 23 G. Longo, L. G. Escrig, M. J. Degen, M. Sessolo and H. J. Bolink, *Chem. Commun.*, 2015, **51**, 7376.
- 24 M. Xiao, F. Huang, W. Huang, Y. Dkhissi, Y. Zhu, J. Etheridge, A. G. Weale, U. Bach, Y. Cheng and L. Spiccia, *Angew. Chem., Int. Ed.*, 2014, **53**, 9898–9903.
- 25 K. Yan, M. Long, T. Zhang, Z. Wei, H. Chen, S. Yang and J. Xu, *J. Am. Chem. Soc.*, 2015, **137**, 4460.
- 26 K. Hwang, Y.-S. Jung, Y.-J. Heo, F. H. Scholes, S. E. Watkins, J. Subbiah, D. J. Jones, D.-Y. Kim and D. Vak, *Adv. Mater.*, 2015, **27**, 1241.
- 27 G. Xing, N. Mathews, S. Sun, S. S. Lim, Y. M. Lam, M. Grätzel, S. Mhaisalkar and T. C. Sum, *Science*, 2013, **342**, 344.
- 28 M. Grätzel, *Acc. Chem. Res.*, 2009, **42**, 1788.
- 29 T. Aernouts, W. Geens, J. Poortmans, P. Heremans, S. Borghs and R. Mertens, *Thin Solid Films*, 2002, **403**, 297.
- 30 C.-H. Chiang, Z.-L. Tseng and C.-G. Wu, *J. Mater. Chem. A*, 2014, **2**, 15897.
- 31 S. Paek, N. Cho, H. Choi, H. Jeong, J. S. Lim, J.-Y. Hwang, J. K. Lee and J. Ko, *J. Phys. Chem. C*, 2014, **118**, 25899.